CrossMark

The Absolute Age of M92

Jiaqi (Martin) Ying[1] , Brian Chaboyer[1] , Emily M. Boudreaux[1] , Catherine Slaughter[1,2] , Michael Boylan-Kolchin[3] , and Daniel Weisz[4]

[1] Department of Physics and Astronomy, Dartmouth College, 6127 Wilder Laboratory, Hanover, NH 03755, USA; martin.ying.gr@dartmouth.edu
[2] Leiden Observatory, Leiden University, NL-2300 RA Leiden, The Netherlands
[3] Department of Astronomy, The University of Texas at Austin, TX 78712, USA
[4] Department of Astronomy, University of California Berkeley, CA 94720, USA

Abstract

The absolute age of a simple stellar population is of fundamental interest for a wide range of applications but is difficult to measure in practice, as it requires an understanding of the uncertainties in a variety of stellar evolution processes as well as the uncertainty in the distance, reddening, and composition. As a result, most studies focus only on the relative age by assuming that stellar evolution calculations are accurate and using age determinations techniques that are relatively independent of distance and reddening. Here, we construct 20,000 sets of theoretical isochrones through Monte Carlo simulation using the Dartmouth Stellar Evolution Program to measure the absolute age of the globular cluster M92. For each model, we vary a range of input physics used in the stellar evolution models, including opacities, nuclear reaction rates, diffusion coefficients, atmospheric boundary conditions, helium abundance, and treatment of convection. We also explore variations in the distance and reddening as well as its overall metallicity and α enhancement. We generate simulated Hess diagrams around the main-sequence turn-off region from each set of isochrones and use a Voronoi binning method to fit the diagrams to Hubble Space Telescope Advanced Camera for Surveys data. We find the age of M92 to be 13.80 ± 0.75 Gyr. The 5.4% error in the absolute age is dominated by the uncertainty in the distance to M92 ($\sim$80% of the error budget); of the remaining parameters, only the total metallicity, α element abundance, and treatment of helium diffusion contribute significantly to the total error.

Unified Astronomy Thesaurus concepts: Globular star clusters (656); Stellar physics (1621); Computational astronomy (293); Stellar evolutionary models (2046)

1. Introduction

Globular clusters (GCs) are stable, tightly bound clusters of stars. They are often modeled as simple stellar populations, as stars in a GC are believed to have the same origin and have similar composition and age. As a result, GCs are an important observational basis for understanding composite stellar populations both inside and outside of the Milky Way as they could be used as building blocks for stellar population synthesis (Bica & Alloin 1986).

GCs are also the oldest objects in the galaxy whose age may be accurately determined. Using JWST data, Mowla et al. (2022) found globular clusters formed at $z > 9$, only $\sim$0.5 Gyr after the Big Bang. Therefore, most GCs are relics of high-redshift star formation and contain the fossil imprint of earliest phases of galaxy formation. Moreover, the bimodality of GCs (each galaxy generally has a metal-poor and a metal-rich subpopulation) permits the investigation of two distinct phases of galaxy assembly (stellar halo and bulge) far beyond the Local Group (Arnold et al. 2011). M92 is one of the oldest and most metal-poor galactic GCs (e.g., Kraft & Ivans 2003). The age of M92, therefore, provides a limit to the age of the universe (Chaboyer 1996) and insights into star formation in the early universe.

Due to its richness, relative proximity, and low reddening, M92 often serves as a benchmark for studies of low-metallicity

stellar systems. For example, Brown et al. (2014) studied the stellar population of six ultrafaint dwarf galaxies (UFDs) using a combination of high-precision photometry data and pointed out that all six UFDs they studied showed that the stars of the smallest galaxies in the universe were formed before reionization because the unusual similarity between their stellar population and that of the M92. As another example of the benchmark nature of M92, it was among the first objects observed with JWST as part of the early release science program 1334 (Weisz et al. 2023).

To first order, stars in a GC can be assumed to form at the same time with the same composition; as a result, theoretical isochrone age fitting is the most widely used method to determine the age of GCs. Theoretical isochrones can be generated by finding the common phase of stellar evolution shared by the stellar evolution model with different masses (Dotter et al. 2008). A variety of methods have been applied to determine the best-fit isochrones for observational data and, therefore, constrain the age of GCs.

Several examples exist for M92. Salaris & Weiss (2002) used the luminosity of the main-sequence (MS) turn-off, combined with the color difference between the turn-off and the base of the giant branch, to find the age of M92 to be 12.3 ± 0.9 Gyr. Using the luminosity of the main-sequence turn-off (MSTO), but a different distance estimate, Carretta et al. (2000) found the age of M92 to be 14.8 ± 2.5 Gyr. Utilizing the shape of the MSTO region as an age indicator, along with a new estimate of distance modulus (DM) and reddening, VandenBerg et al. (2002) estimated the age of M92 to be 13.5 ± 1.0 Gyr. Cecco et al. (2010) combined data from

Table 1
Monte Carlo Input Parameters

Variable	Distribution	Range	Source
[Fe/H]	Normal	-2.30 ± 0.10	Kraft & Ivans (2003)
			Carretta et al. (2009)
			Cohen (2011)
Primordial helium abundance	Uniform	0.244–0.249	Aver et al. (2015)
[α/Fe]	Normal	0.40 ± 0.1	Roederer & Sneden (2011)
Mixing length	Uniform	1.0–2.5	N/A
Heavy element diffusion	Uniform	0.5–1.3	Thoul et al. (1994)
Helium diffusion	Uniform	0.5–1.3	Thoul et al. (1994)
Surface boundary condition	Trinary	1/3; 1/3; 1/3	Eddington (1926)
			Krishna Swamy (1966)
			Hauschildt et al. (1999)
Low-temperature opacities	Uniform	0.7–1.3	Ferguson et al. (2005)
High-temperature opacities	Normal	1.0 ± 0.03	Iglesias & Rogers (1996)
Plasma neutrino loses	Normal	1.0 ± 0.05	Haft et al. (1994)
Conductive opacities	Normal	1.0 ± 0.20	Hubbard & Lampe (1969)
			Canuto (1970)
Convective envelope overshoot	Uniform	0–0.2	N/A
Convective core overshoot	Uniform	0–0.2	N/A
$p + p \rightarrow H_2 + e + \nu$	Normal	$(4.07 \pm 0.04) \times 10^{-22}$	Acharya et al. (2016)
			Marcucci et al. (2013)
$^{3}He + {}^{3}He \rightarrow {}^{4}He + p + p$	Normal	5150 ± 500	Adelberger et al. (2011)
$^{3}He + {}^{4}He \rightarrow {}^{2}H + \gamma$	Normal	0.54 ± 0.03	deBoer et al. (2014)
$^{12}C + p \rightarrow {}^{13}N + \gamma$	Normal	1.45 ± 0.50	Xu et al. (2013)
$^{13}C + p \rightarrow {}^{14}N + \gamma$	Normal	5.50 ± 1.20	Chakraborty et al. (2015)
$^{14}N + p \rightarrow {}^{15}O + \gamma$	Normal	3.32 ± 0.11	Marta et al. (2011)
$^{16}N + p \rightarrow {}^{17}F + \gamma$	Normal	9.40 ± 0.80	Adelberger et al. (2011)

Note. We adopt a -3σ lower boundary for all physics-based parameters with normal distribution to prevent nonphysical results (such as a negative nuclear reaction rate). Units for nuclear reaction rates are keV-barns. Convective parameters are given in units of pressure scale heights. [Fe/H] and [α/Fe] have their standard logarithmic definition with respect to the solar value. The primordial helium abundance is given as a mass fraction. All other parameters are multiplicative about the standard value given in the source column.

three different photometric systems—Sloan Digital Sky Survey (SDSS), Johnson-Kron-Cousins, and Advanced Camera for Surveys (ACS)—and, using the morphology and number counts of stars in the MSTO, red giant branch, and horizontal branch, found the age of M92 to be 11 ± 1.5 Gyr. Marín-Franch et al. (2009) derived ridge lines in the color–magnitude diagram (CMD) from the ACS data to perform relative MS fitting between clusters and found the age of M92 to be 13.18 ± 0.51. In general, the uncertainty in age determinations for GCs typically takes into account the uncertainties in the observed properties of a globular cluster (distance, reddening, and composition), but do not include the uncertainty associated with the theoretical stellar models and isochrones which are used to determine the age.

Modern stellar evolution codes can generate theoretical stellar models quickly for a wide range of initial conditions. Theoretical isochrones are sensitive to the input parameters used to generate these stellar models. Most previous studies using theoretical isochrones are limited in that they do not take into consideration the wide range of uncertainty in constructing stellar models. In this paper, we utilize a Monte Carlo (MC) approach to generate uncertainties in theoretical isochrones. We generate isochrones by varying various input physics in the stellar evolution models. For a given stellar model, we will prescribe its mass and heavy element composition and then vary the opacities, nuclear reaction rates, microscopic diffusion coefficients, atmospheric boundary conditions, helium abundance, and treatment of convection. All those parameters

(shown in Table 1) are varied during the MC simulation based on their known uncertainties. The resultant isochrones provide a good estimation of the uncertainty associated with modern stellar evolution calculations.

A variety of methods have been used to compare theoretical isochrones to observational data in order to determine the age of a stellar population. Typically, certain age-sensitive aspects of the observed CMD are compared to stellar models/ isochrones. The MSTO region is particularly sensitive to age and is therefore often used to determine the ages of GCs (e.g., VandenBerg et al. 2002). However, the morphology of the horizontal branch has also been used in measuring GC ages (e.g., Salaris & Weiss 2002; Cecco et al. 2010). VandenBerg et al. (2016) used both the MSTO region and the horizontal branch to determine the age of a few globular clusters, including M92. These previous studies have focused on comparing the shape/morphology of the observational data to theoretical isochrones in order to determine their age.

In this paper, we present a new isochrone age fitting method that uses Voronoi binning and fits the number density of stars in the MSTO region to determine ages. By utilizing the density of stars in the CMD (usually referred to as a Hess diagram) to determine the age of a cluster, we utilize all of the observational information to constrain the age. This may lead to smaller uncertainties compared to previous work. This paper is structured as follows. In Section 2, we introduce the observational data; Section 3 covers the process of isochrone construction; Section 4 presents the details of our isochrone age

fitting method and our best age measurement; and Section 5 includes a discussion of the sources of error and covariance.

2. Observational Data

2.1. Calibration Stars

There are two single, metal-poor main-sequence stars that have accurate Hubble Space Telescope (HST) ACS photometry (in the same filters as the M92 ACS data) and virtually the identical composition as M92: HIP 46120 and HIP 106924. The HST photometry is presented in Chaboyer et al. (2017) and the high-resolution spectroscopic abundances in O'Malley et al. (2017). These two stars have accurate Gaia EDR3 parallaxes of 14.776 ± 0.014 mas and 15.019 ± 0.012 mas respectively (Lindegren et al. 2021a; Gaia Collaboration et al. 2021).

The EDR3 parallaxes are known to suffer from systematic zero-point errors, and a calibration of this error has been given by Lindegren et al. (2021b). This correction is -0.012 mas for HIP 46120 and -0.020 mas for HIP 106924. However, the zero-point correction is not that well calibrated for bright stars like these two stars (Lindegren et al. 2021b) and there is evidence that the zero-point correction may be an over-correction for bright stars (Riess et al. 2021; Zinn 2021) so we elected to add in half the zero-point correction to the quoted EDR3 parallax. The uncertainty in the parallaxes was taken to be the value of the zero-point correction added in quadrature with the uncertainty in parallax given in EDR3.

Combining the parallaxes with the HST ACS photometry, we measure $M_{F606W} = 5.7867 \pm 0.0026$ mag for HIP 46120 and $M_{F606W} = 6.0406 \pm 0.0037$ mag for HIP 106294. These stars have zero reddening (O'Malley et al. 2017) and observed colors of (F606W-F814W) $= 0.566 \pm 0.002$ and (F606W-F814W) $= 0.601 \pm 0.005$. These accurate colors and absolute magnitudes will be used to test the isochrones in Section 3.1.

2.2. M92

To estimate the age of M92, we use calibrated data for M92 from the Hubble Space Telescope (HST) Advanced Camera for Surveys (ACS) globular cluster survey treasury program (Sarajedini et al. 2007; Anderson et al. 2008). The survey obtained photometry with a signal-to-noise ratio (S/N) >10 for main-sequence stars with masses $>0.2\,M_\odot$ using the ACS Wide Field Channel. Artificial star tests provide an accurate estimate of the photometric uncertainties and completeness as a function of magnitude and cluster position (Anderson et al. 2008). Since this paper focuses on determining the age of M92, we use a subset of stars around the MSTO to fit isochrones whose position is most sensitive to variations in age, and relatively insensitive to the present-day mass function. These stars have a $15.925 < F606W < 19.925$, which is ± 2 magnitudes of the point on the subgiant branch which is 0.05 mag redder than the MSTO. Additionally, we remove blue straggler stars and outliers by selecting stars that are within 0.08 mag in F606W of the median ridgeline in a magnitude–magnitude diagram of F814W and F606W. With these cuts, our observational sample contains 18, 077 stars.

We note that previous studies (e.g., Mészáros et al. 2015; Milone et al. 2017) demonstrate that M92, like other old globular clusters, hosts multiple stellar populations. These multiple stellar populations typically have somewhat different lighter element abundances, the origin of which is not currently known. These multiple populations are observed in UV filters such as F275W and F336W from the HST. However, these populations are indistinct from each other in the F606W and F814W data used in this paper. As a result, these multiple populations will not be considered in this study.

3. Isochrone Construction and Testing

We use the Dartmouth Stellar Evolution Program (DSEP; Dotter et al. 2008) to generate stellar models and isochrones and generally use literature estimates when adopting uncertainties for each parameter (see Table 1). One area where we consider a wider range of uncertainties is in the treatment of convection: even though nearly all models use a solar-calibrated mixing length, a variety of studies have demonstrated that this may not be the most appropriate value for other stars. Joyce & Chaboyer (2018) studied metal-poor stars including M92 and discovered that the solar-calibrated value of the mixing length parameter α_{MLT} was ineffective at reproducing their observed properties. As a result, we adopt a wider input range for the mixing length parameter α_{MLT} to cover the range of empirically calibrated mixing length parameter α_{MLT}. Another source of uncertainty associated with the treatment of convection in stellar models is the amount of convective overshoot, which may occur at the formal edge of a convection zone (which is defined by the buoyancy force being zero). Various studies have calibrated the amount of convective overshoot by comparing to observations (e.g., Claret 2004; Demarque et al. 2004; Pietrinferni et al. 2004; Mowlavi et al. 2012). In general, these studies have found a fairly small value of 0.0–0.2 pressure scale heights; we therefore adopt this range for convective overshoot in our analysis.

We generate 20,000 sets of input parameters by doing Monte Carlo simulations on parameters shown in Table 1 from their associated probability distribution functions. Each set of input parameters is used to evolve 21 stellar models with mass from $0.65\,M_\odot$ to $1.5\,M_\odot$ with an increment of $0.05\,M_\odot$ and 12 lower-mass stellar models with mass from $0.3\,M_\odot$ to $0.63\,M_\odot$ with an increment of $0.03\,M_\odot$. The lower-mass models use the FreeEOS-2.2.1 (Irwin 2012), while the higher-mass models use an analytical equation of state which includes the Debyre–Huckel correction (Chaboyer & Kim 1995). These stellar models are used to generate 41 theoretical isochrones from 8 Gyr to 16 Gyr with an increment of 200 Myr. Those 41 isochrones of different ages corresponding to the same set of MC input parameters are considered a single MC isochrone set. Each isochrone is constructed with a dense grid of 400 equal evolutionary points in order to ensure that the output isochrones have a high density of points to avoid any interpolation errors when constructing simulated color–magnitude diagrams (sCMDs).[5] In summary, we generated 20,000 isochrone sets. Each isochrone set consists of 41 isochrones of different ages, for a total of 20,000 ×41=820,000 individual isochrones. Figure 1 shows the distribution of all 20,000 13 Gyr isochrones generated for this project. The extensive range covered by the single age isochrones in the color–magnitude plane affirms our hypothesis that varying the MC input parameters can significantly influence the resulting isochrones. Hence, it is imperative to take into account the uncertainty in

---

[5] The Monte Carlo isochrones created for this project are available at https://doi.org/10.5281/zenodo.7758605. The file is stored in HDF5 format, and a sample Python program is provided which gives details on extracting isochrones from the HDF5 file.
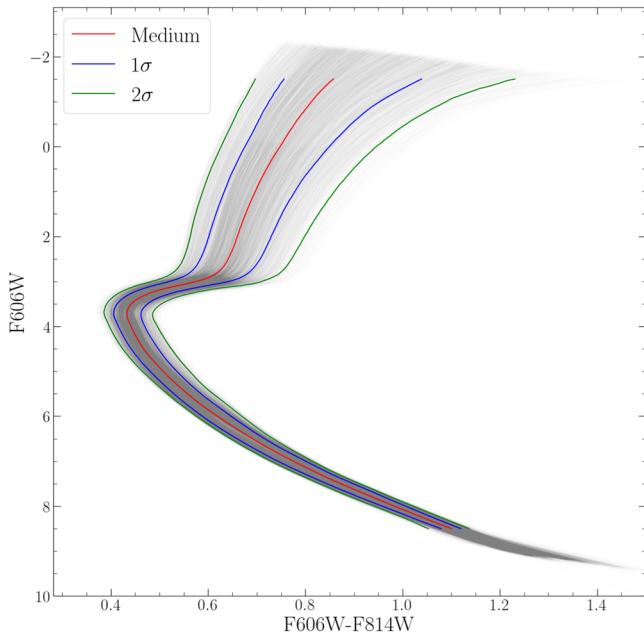
Figure 1. An illustration of the 20,000 13 Gyr MC isochrones (gray) generated for this project. The red curve is the interpolated isochrone which is selected by taking the median F606W-F814W value of all isochrones at a given F606W value. The corresponding 68% confidence intervals and 95% confidence intervals are shown in blue and green curves, respectively.

these parameters when providing an accurate determination of the age of M92.

3.1. Testing the Isochrones

As HIP 46120 and HIP 106924 have known absolute magnitude and colors, and nearly identical compositions to M92, these stars provide an empirical baseline for an isochrone goodness-of-fit metric. Specifically, we perform a χ^2 goodness-of-fit test between the two calibrating stars and each age of each MC isochrone set. The lowest χ^2 value for a given MC isochrone set is then used to compute a weighting function for that entire set of MC isochrones (i.e., for a given MC isochrone set, we assume the best-fitting isochrone gives an indication of the age of the calibrating star, which may be different from the age of M92). Essentially, how well any given MC isochrone set fits to the observed calibration data will determine the weight that an MC isochrone from that set is given when fitting to M92. We use the inverse of the probability that a given MC isochrone is inconsistent with the calibration data as the weighting function.

We define the χ^2 metric for each isochrone as the quadrature sum of the differences between that isochrone's and calibrating star's F606W magnitude and F606W-F814W color. In order to account for uncertainty in the calibrating stars photometry the differences used are normalized by the magnitude and color uncertainties. χ^2 is found for each age in each of the 20,000 sets of isochrones. The age with the minimum χ^2 is then selected for each set of isochrones. From these minimized χ^2 values, we directly compute the weighting function.

The two calibrating stars provide 2° of freedom, n, for the χ^2 distribution; in the case where $n = 2$, the cumulative distribution function (CDF) for a χ^2 distribution is given by
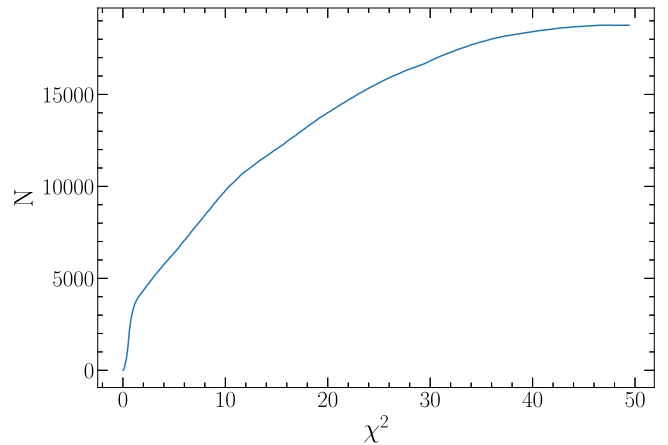
$$CDF = 1 - e^{-x/2}. \tag{1}$$

Figure 2. The cumulative distribution of the minimum χ^2 values for all MC isochrones.
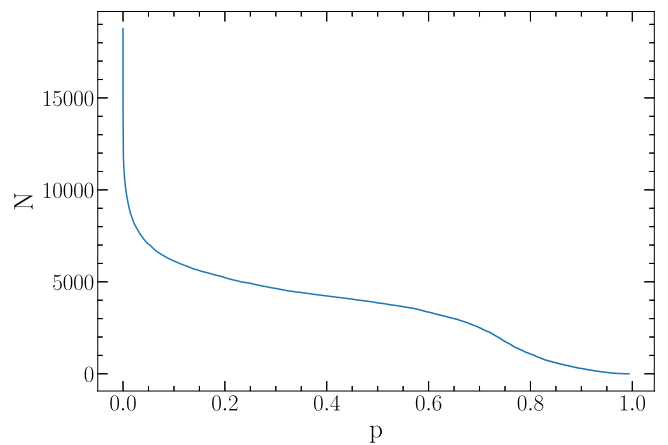

Figure 3. The distribution of the weight p for 20,000 sets of MC isochrones.

The weighting function used, p, for any given isochrone, is then

$$p = 1 - CDF. \tag{2}$$

Figure 2 shows the cumulative distribution of minimized χ^2 values, and Figure 3 shows the cumulative distribution of the weight p for 20,000 sets of MC isochrones. Approximately 20% of the isochrone sets have $\chi^2 < 2$ and so provide a good fit to the calibration stars. Only about 35% of the isochrone sets have a CDF <0.95, which corresponds to a weighting function >0.05%.

3.2. Simulated Color–magnitude Diagram

Each MC set of theoretical isochrones is used to create a set of sCMDs of M92 which will be used to compare with the observational CMD of Sarajedini et al. (2007). An sCMD is constructed by randomly creating a 4 million-point sample for each isochrone in the following steps:

1. A random distance from the center of the cluster is selected from the observed distribution (Sarajedini et al. 2007).
2. A random mass is selected using the present-day mass function determined by Paust et al. (2010), who found a power-law mass function with a slope of −1.02 using the same ACS M92 data. The magnitudes (F606W and

F814W) of this simulated star are then determined from the isochrone.

3. The simulated star is randomly assigned to be a member of a binary system, using the observed binary mass fraction of 0.02 (Milone et al. 2012).
4. If a star is a member of a binary system, then a secondary star is created, assuming a flat secondary mass distribution with a mass ratio $q = 0.5$–1.0. The magnitudes of this secondary star are determined from the isochrone and added to the magnitude of the primary to arrive at the magnitude of the binary star system; which is considered to be a single star in the photometry.
5. It is determined if the star would be recovered in the photometric reduction, using the photometric completeness function from (Anderson et al. 2008) for the M92 ACS data. This photometric completeness function depends on the magnitudes of the star and its distance from the center of the cluster.
6. If the star is found to be observable in the previous step, then photometric errors will be randomly selected from their observed distribution (which is a function of magnitude and distance from the cluster center). The observed distribution of photometric errors is determined from the artificial star tests of Anderson et al. (2008).
7. The photometric errors in F606W and F814W are added to the magnitude of the simulated star, and these magnitudes are used in creating the sCMD.

Once the sCMD is created, the same color and magnitude filters that were applied to the observed M92 data are applied to the sCMD. After this filtering, the sCMD consists of about 2 million simulated data points for each theoretical isochrone.

We note that after we completed our age determination for M92, we discovered that Ebrahimi et al. (2020) found a strong correlation between the distance from the center of the GC and the present-day mass function (PDMF) slope. Ebrahimi et al. (2020) found a PDMF slope in the inner region of M92 which ranged from -1 to $+2$, while our sCMD assumed -1.02 (Paust et al. 2010). Since we are only fitting stars that are around the MSTO, which all have similar masses, the exact PDMF slope should have little impact on our results. To test this, we created sCMDs with PDMF slopes ranging from -2.02 to 1.02 and found the change in PDMF slope indeed had a negligible impact on the estimated age for M92.

4. Isochrone Fitting

To estimate the age of M92, each sCMD is compared to the observational CMD, and the fit probability is calculated. In order to compare CMDs, we divide the 2D CMD into multiple subsections and estimate the goodness of fit using a χ^2 method:

$$\chi^2 = \sum_i \frac{(O_i - E_i)^2}{E_i}, \qquad (3)$$

where E_i is the number of data points in a subset of the CMD in the observational data and O_i is the number of sampled data points in the same subset from the sCMD. Since the number of stars in the sCMD is $\sim$100 times larger than the number of stars in the observed CMD, the uncertainty in the number counts for simulated stars is negligible in comparison to the uncertainty in the number counts for the observed stars. The

age determination is done in a series of steps, as discussed below.

4.1. Voronoi Binning

To compare the sCMD with the observational CMD, a method to partition the 2D CMD was required. The most intuitive method will be dividing the CMD using a uniform grid. However, the distribution of stars in the CMD is highly biased. As a result, if the bins of a 2D CMD were defined by evenly spaced grids, there would be a wide distribution of expected data points in each bin, with some bins being empty (either in the real, or simulated data). Therefore Equation (3) could not be used for that bin. A better approach of a nonuniform partition of the 2D CMD results in a roughly equal number of points per bin is required.

To achieve this requirement, we use the adaptive Voronoi binning method of Cappellari & Copin (2003). The algorithm sets up initial bins based on a Voronoi Tessellation formed by the simulated CMD. It iteratively combines bins nearby and thus raises the S/N until it reaches the target. It satisfies three requirements:

1. Topological requirement: there will be no data points that are not in a bin, and no bins overlap,
2. Morphological requirement: the bin shape will be as "compact" (or "round") as possible so that two pixels from two corners across the CMD will not be put into one bin,
3. Uniformity requirement: the resulting bins will have a similar number of data points as targeted. Therefore, all bins can be considered as having equal statistical significance.

This Voronoi binning is extremely computationally demanding, and to save CPU time, 180, 000 points from each sCMD are randomly selected to generate Voronoi bins. Each set of Voronoi bins contains 800 bins with an average of 225 points in each bin. Because the Voronoi binning method of Cappellari & Copin (2003) was designed to deal with images and required the pixel size to be the same on both axes, we rescaled the magnitude of F606W-F814W before doing the Voronoi binning. Because the linear transformation does not change the topology of the data, the original data can be easily recovered for further analysis. Different combinations of a number of data points used and a number of Voronoi bins were tested and the combination being used in this paper shows a balance in computational time and accuracy. After the Voronoi bin is determined, the entire sCMD will be binned and contribute to the expectation in Equation (3).

Figure 4 shows an example of Voronoi binning (Cappellari & Copin 2003). The CMD is divided into 800 different subsets with different sizes. Most bins locate near the isochrone (red line) and few bins locate outside where the density of simulated data points (blue dots) is low.

For each set of Voronoi bins, the observational CMD is shifted by a range of distance modulus and reddening, with the ranges chosen to encompass the observed uncertainties in these quantities. The distance to M92 is estimated using main sequencing fitting using the two calibration stars which are good HST photometry and parallaxes from Gaia EDR3 (Collaboration et al. 2021). Assuming a reddening of $E_{F606W-F814W} = 0.02$, the distance modulus of $(m - M)_{F606W} = 14.80 \pm 0.02$ is found. Assuming a reddening
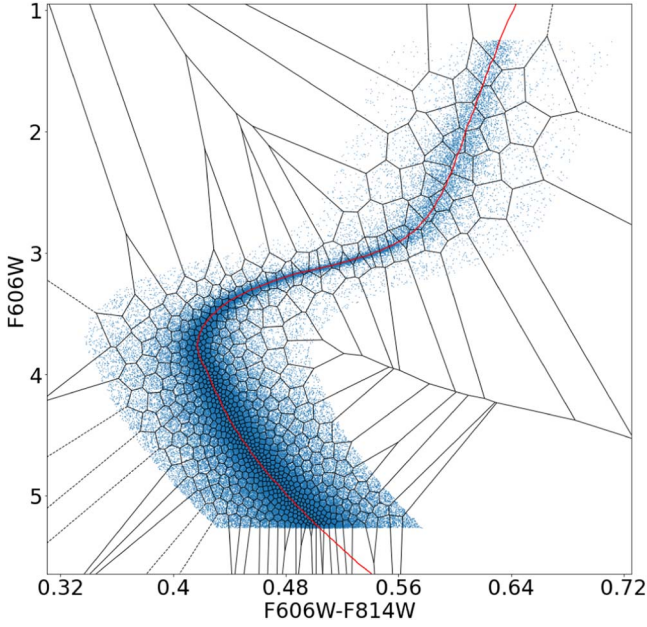
Figure 4. An example of the result of the adaptive Voronoi binning method (Cappellari & Copin 2003). The CMD is divided into 800 different subsets. Blue dots are the 180,000 data points used to generate the Voronoi tessellation. The red curve is the isochrones used to simulate the CMD.
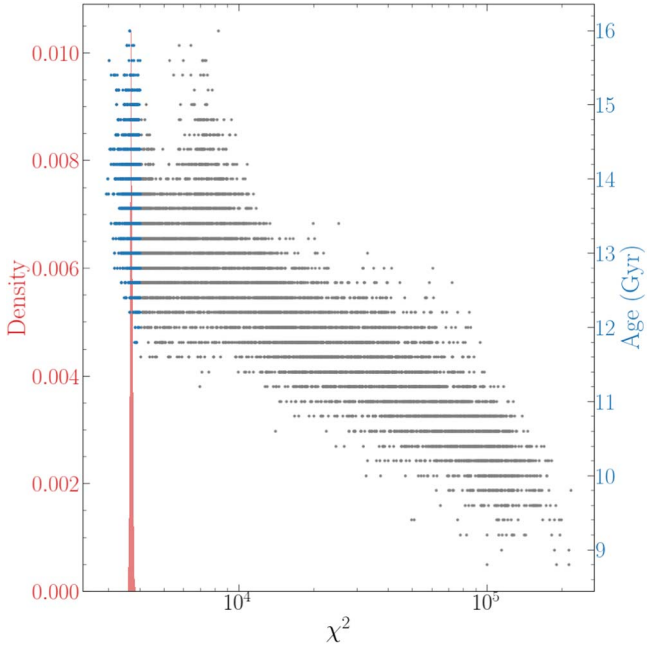

Figure 6. The empirical χ^2 distribution is shown in red, while the χ^2 values determined from fitting the MC isochrones to M92 are shown in blue (as a function of age). Only the 1100 isochrones which are within 3σ of the mean of the empirical distribution are shown in this figure. The x-axis is in linear scale.

distance modulus of $(m - M)_V = 14.82$ and $E_{B-V} = 0.025$ from fitting a different set of isochrones to a different ground-based data set. Baumgardt & Vasiliev (2021) used a variety of methods (including EDR3 parallaxes of cluster stars, and main-sequence fitting) to estimate distance to M92 to be 8.48 ± 0.17 kpc which is $(m - M)_o = 14.64 \pm 0.04$. Assuming a reddening of $E_{B-V} = 0.01$, this corresponds to $(m - M)_{F606W} = 14.67$. Based upon the above, the distance modulus used in this paper range from 14.62 to 14.82 with an increment of 0.01, and the reddening range from 0.0 to 0.05 with an increment of 0.01. For each combination of distance modulus and reddening, a χ^2 value was calculated using Equation (3) for each of the 41 ages in each MC isochrone set. The minimum χ^2 was then selected as the best estimate of the age, distance modulus, and reddening for that particular MC isochrone.

Figure 5. The distribution of χ^2 values found using Equation (3) when comparing the sCMDs to the observed data. The empirical χ^2 distribution is shown in red, and the χ^2 values found when fitting the M92 data to the MC isochrones are shown as a function of age (scale shown on the right vertical axis). The 1100 isochrones which are within 3σ of the mean of the empirical distribution are shown as blue dots. The remaining isochrones have $\chi^2 > 4100$ and are shown as gray dots. Note that the x-axis is on a logarithmic scale.

4.2. Empirical χ^2 Distribution

Lin et al. (2013) demonstrated that with large data sets, using the p-value-based hypothesis testing method no longer provides scientifically reliable results. Therefore, with the M92 data, it is inappropriate to estimate the goodness of fit using the standard χ^2 fit probability function. To interpret χ^2 values calculated in Section 4.1, a statistical method to determine the empirical χ^2 distribution is required. To do so, we resample the observational data using the photometric error and completeness from the artificial star test (Anderson et al. 2008). From the observed data, 10, 000 CMDs each with about 2 million data points are generated. Using the same method described in Section 4.1, for each resampled CMD, a set of Voronoi bins is determined and a χ^2 value is calculated using Equation (3). As a result, an empirical χ^2 distribution is determined and is used to compare with theoretical values.

of $E_{F606W-F814W} = 0.01$, the main-sequence fitting yields a distance modulus of $(m - M)_{F606W} = 14.75 \pm 0.02$. The evidence favors the higher reddening value. An independent distance estimate to M92 by VandenBerg et al. (2002) is $(m - M)_V = 14.62$ and $E_{B-V} = 0.023$ based upon fitting ground-based data to their isochrones (which assumes no uncertainty in their isochrones). Cecco et al. (2010) found a
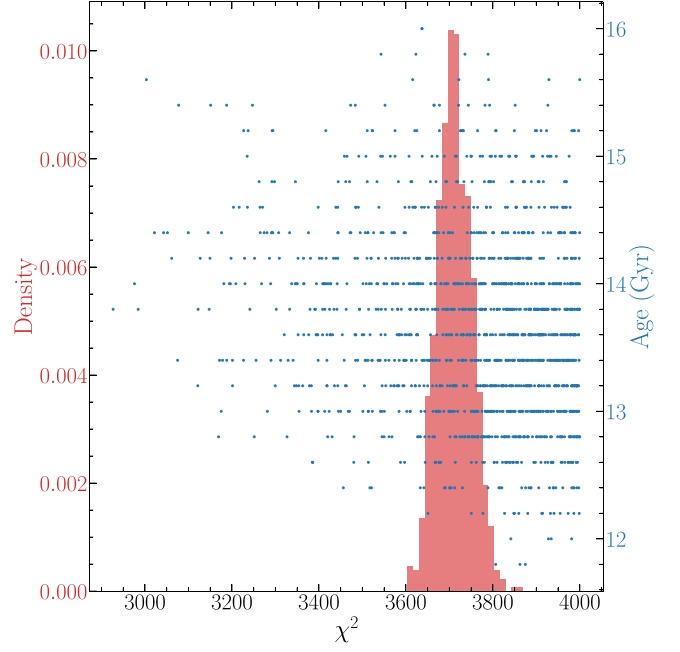
Figure 5 shows the empirical χ^2 distribution and the χ^2 values determined when comparing the MC isochrones to the observations. From the 20,000 sets of theoretical isochrones
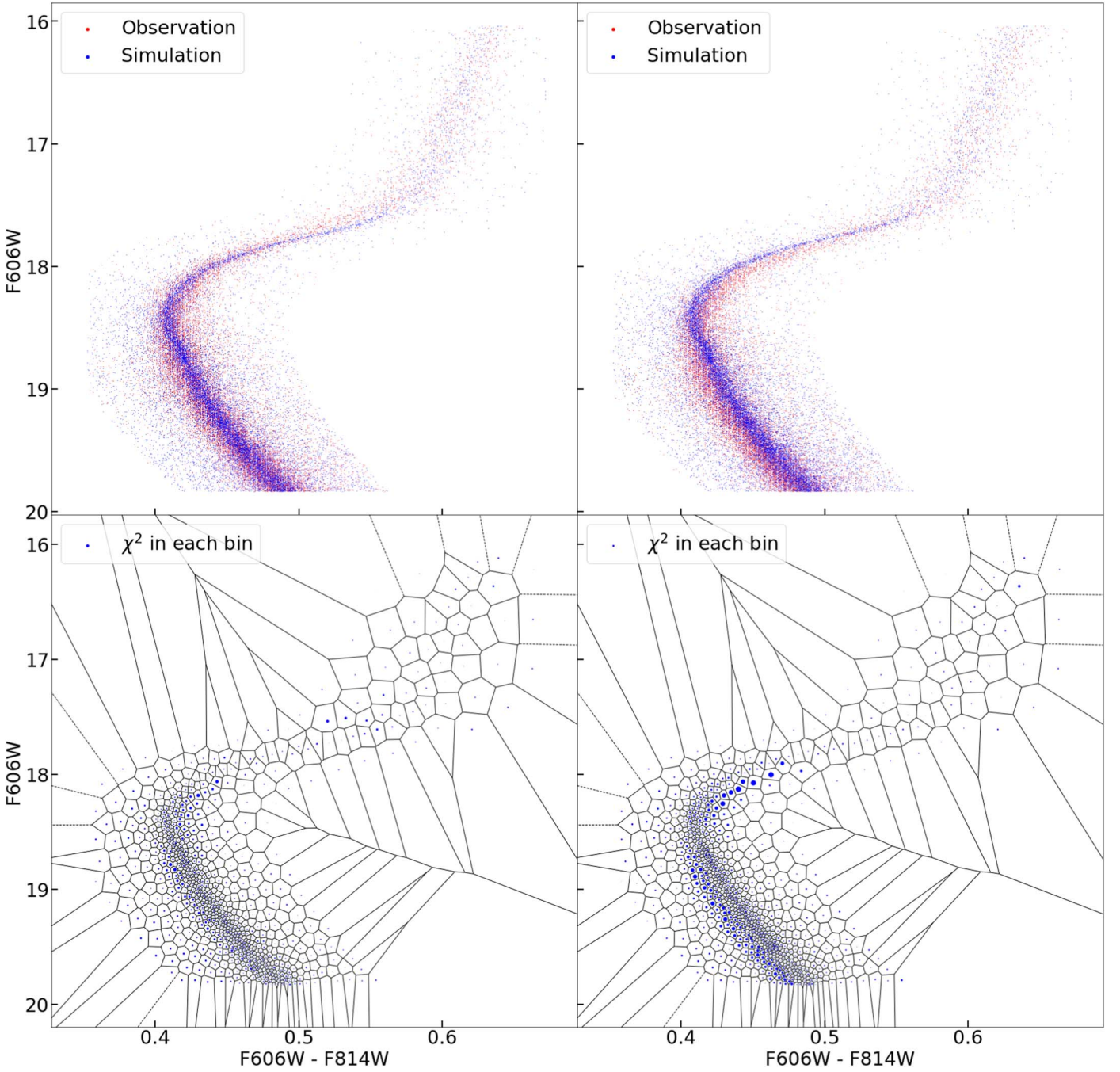
Figure 7. Top left (a): an example of a "high probability fit" for M92. The χ^2 value is within 1σ of the mean of the empirical distribution. Blue dots are parts of the sCMD and red dots are observed data for M92. Top Right (b): an example of "low probability fit" for M92. The χ^2 value is almost 3σ greater than the mean of the empirical distribution. Blue dots are parts of the sCMD and red dots are observed data for M92. Bottom left (c): an example of "high probability fit" for M92. The size of the blue dots indicates the χ^2 value for the Voronoi bin they located at. Bottom Right (d): an example of "low probability fit" for M92. The size of the blue dots indicates the χ^2 value for the Voronoi bin they located at.

created in this study, 1100 isochrones are within 3σ of the mean of the empirical distribution. The other 18,900 MC isochrones yielded a very poor fit to the observed data. Figure 6 is a zoomed-in version of Figure 5 and shows 1100 isochrones are within 3σ of the mean of the empirical distribution. Most of these 1100 isochrones also provided a good fit to the calibration star data. However, 66 of the isochrones provided relatively poor fits to the calibration stars, leading to a calibration star weighting value of less than 0.10. The shape of the empirical χ^2 distribution can be fit with a normal distribution $\chi^2 = 3712 \pm 39$ and spans a very narrow region in χ^2.

Figure 5 shows that the mean of the empirical χ^2 distribution can be several orders of magnitude smaller than the χ^2 of isochrones which poorly fits the data, which shows the sensitivity of isochrones to MC parameters and the selectivity of our age determination technique. Figures 7(a) and (b) show examples of the sCMDs which are generated from those 1100 theoretical isochrones. Figure 7(a) has a χ^2 value that is within 1σ of the mean of the empirical distribution and is considered a "high probability fit" for M92, with a higher weight in the final age estimation. Figure 7(b) has a χ^2 value which is almost 3σ greater than the mean of the empirical distribution and is
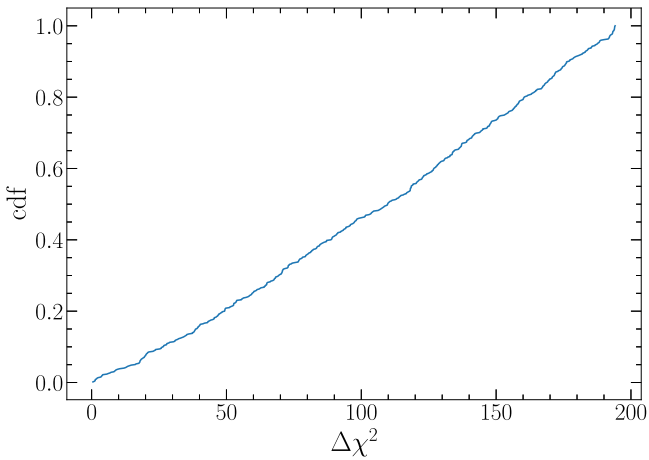
Figure 8. The cumulative distribution function of the χ^2 values which are higher than the mean of the empirical χ^2 distribution while being within 3σ of the mean of the empirical distribution.
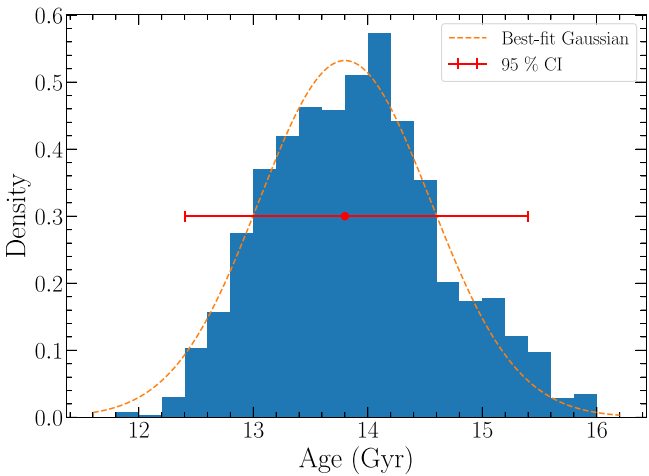

Figure 9. The weighted distribution of ages corresponding to best-fit isochrones (blue histogram). The orange curve represents the best-fit Gaussian model, $\mathcal{N}(13.80, 0.75)$. The 95% confidence interval of the estimated age is (12.4, 15.4) Gyr.

considered a "low probability fit" for M92. Although it is taken into consideration in the age estimation, it had a much lower weight.

Figures 7(c) and (d) are the corresponding χ^2 values for each of the Voronoi bins of the two sCMDs shown in Figures 7(a) and (b), respectively. Figures 7(c) and (d) show a difference mostly in the main sequence and MSTO which favors the sCMD shown in Figure 7(a).

4.3. Age Estimation

Figure 5 shows a clear bias toward χ^2 values higher than the mean of the empirical χ^2 distribution. As a result, the χ^2 values smaller than the mean of the empirical χ^2 distribution were considered to have a "fit probability" of 1 while the "fit probability" of χ^2 values higher than the mean of the empirical χ^2 distribution was defined by the empirical χ^2 distribution where the cumulative distribution function is shown in Figure 8.

The "fit probability" from the empirical χ^2 distribution was multiplied by the probability found in Section 3.1 to result in a final weight for each of the 1100 isochrones. The age
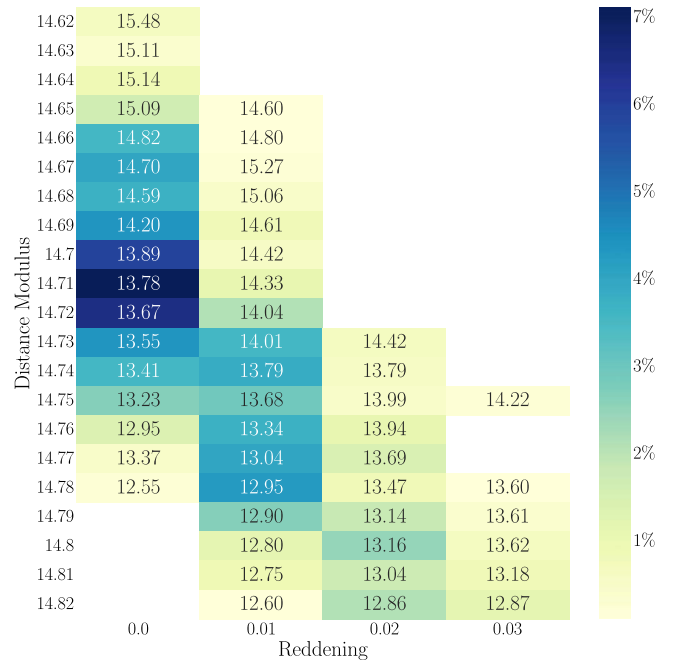

Figure 10. The best-fit age corresponding to each combination of distance modulus and reddening. The annotation on each block represents the estimated age (Gyr) from each combination. The color represents the occurrence of each combination as a percentage of the total 1100 best-fit isochrones. 78 out of the 1100 best-fit isochrones choose distance modulus =14.71 and reddening = 0.0 with an estimated age of 13.78 Gyr.

distribution is shown in Figure 9. The weighted average of the age of the 1100 isochrones is equal to 13.80 Gyr and the weighted standard deviation is 0.75 Gyr. Thus, we measure the absolute age of M92 to be 13.80 ± 0.75 Gyr. At 95% confidence, we find the age to be in the range 12.4–15.4 Gyr.

5. Discussion

5.1. Distance Modulus and Reddening

As described in Section 4.1, we tested distance moduli ranging from 14.62 to 14.82 (with an increment of 0.01) and reddening ranging from 0.0 to 0.05 (with an increment of 0.01) for each isochrone. The best-fitting age corresponding to each distance modulus and age is shown in Figure 10. This figure clearly (and unsurprisingly) indicates that the lower best-fit age favors a higher distance modulus. The Pearson correlation coefficient between the distance modulus and best-fit age $= -0.780$, indicating a strong negative correlation between the distance modulus and the best-fit age. This result is expected: a higher distance modulus will shift the theoretical isochrone in the sCMD in the opposite direction of a shift in the sCMD due to a lower isochrone age and will remain close to the true distribution of stars observed in M92. Figure 10 also shows a strong preference toward lower reddening values.

The weighted average of distance modulus is $\mu = 14.72 \pm 0.04$ mag ($D = 8.79 \pm 0.16$ kpc), which is similar to Carretta et al. (2000), but lower than Cecco et al. (2010) and slightly higher than Baumgardt & Vasiliev (2021), who found $\mu = 14.66 \pm 0.04$. Our result has a strong preference toward a low reddening: there are no well-fitting isochrones with $E(B - V) = 0.04$ or 0.05. Since the distribution of reddening is nonsymmetric, we select the central 68% of the distribution and find that the reddening of M92 is in the range E

Table 2

Source	Age (Gyr)	Distance Modulus μ (mag)	Reddening $E(B-V)$ (mag)
This paper	13.80 ± 0.75	14.72 ± 0.04	$0.005 \sim 0.025$
Carretta et al. (2000)	14.8 ± 2.5	14.74 ± 0.07	0.025 ± 0.005
VandenBerg et al. (2002)	13.5 ± 1.0	14.62	0.023
Cecco et al. (2010)	11.0 ± 1.5	14.82	0.025 ± 0.010
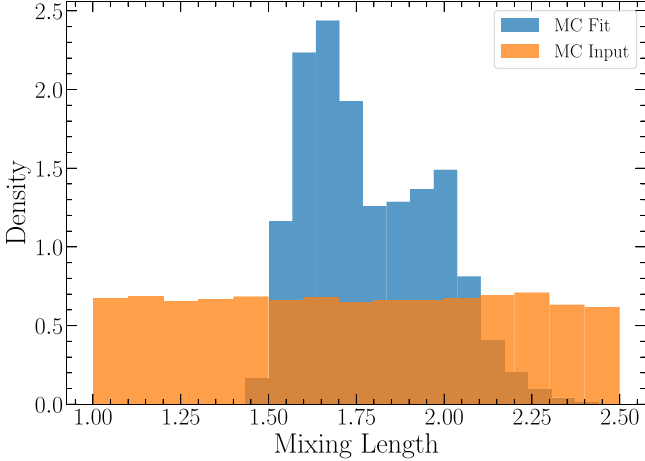
Figure 11. The distribution of mixing length as an input parameter (see Table 1). The solar-calibrated mixing length used as the median set of MC parameters is 1.75.
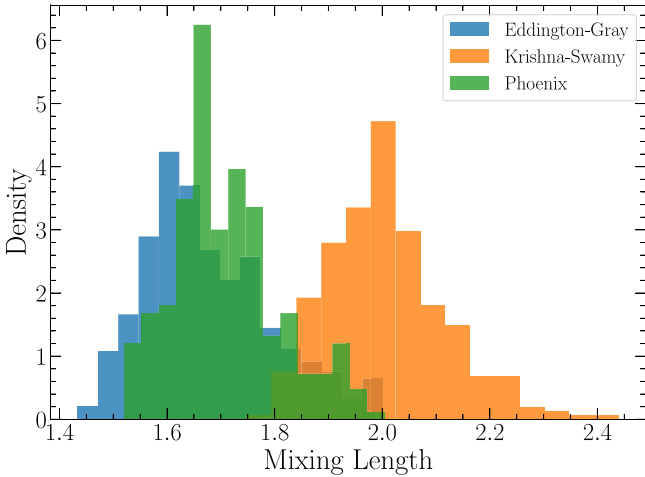
Figure 12. The distribution of mixing length from the 1100 sets of best-fit isochrones for all three models of atmosphere used.

$(B - V) = 0.005$–0.025 mag, with the distribution skewed to smaller reddening values. This is within the range of previous results as shown in Table 2.

Most of the studies on GC age dating (e.g., Carretta et al. 2000; Salaris & Weiss 2002) rely mainly on MSTO stars to determine the age of a cluster. However, we include a wider range of stars with F606W magnitude from 15.925 to 19.925. As a result, our study includes not only MSTO stars but also a subset of stars lying on the main sequence (MS) and giant branch (GB). Although MS stars and GB stars are not very sensitive to age, we include them in this study to constrain the distance modulus and reddening of M92.

To test this idea, we applied the method described in Section 3.2 and Section 4 to M92 data with only MSTO stars. Due to computational limitations, we generated and fitted 2,

000 sets of sCMDs (1000 of which had been found to be good fits in our previous analysis, and 1000 which were poor fits in our previous analysis). By exclusively using MSTO stars, we were able to determine the age of M92 as $=13.88 \pm 0.81$ Gyr with distance modulus $\mu = 14.68 \pm 0.05$ and reddening $E(B - V) = 0.005$–0.045. These results, which exhibit a slightly higher age and larger uncertainty compared to those in Table 2, follow expectations: removing MS and GB stars provides more freedom in selecting distance modulus and reddening, thus partially offsetting the impact of the change in isochrone age. In this case, we suggest that the wider range of best-fit reddening values is the cause of the higher uncertainty in age estimated and the slightly lower distance modulus value is likely due to the strong negative correlation between it and the age.

5.2. Monte Carlo Parameters

To determine if the observational data is best fit by a limited range in our MC parameters, we compare the distribution of input MC parameters (see Table 1) to the distribution of the MC parameters in the set of 1100 best-fit isochrones. Most parameters have similar distributions, while differences are found for a few parameters. For example, the distribution of the mixing length is shown in Figure 11. While a uniform distribution from 1.0 to 2.5 was used as input, the best-fitting isochrones show a very strong preference for mixing length values between 1.5 and 2.0.

The value of solar-calibrated mixing length depends strongly on the surface boundary conditions which are used in constructing a stellar model. The correlation between the mixing length and surface boundary condition for the 1100 sets of best-fitting isochrones is shown in Figure 12. DSEP determines the conditions at the surface of the star using model atmospheres. The three options used in the MC were PHOENIX model atmospheres (based upon a sophisticated radiative transfer code; see Hauschildt et al. 1999) which has a solar-calibrated mixing length of 1.7, the simple Eddington gray model atmosphere which has a solar-calibrated mixing length $\alpha_{MLT} = 1.7$, and the empirical solar Krishna Swamy atmosphere which has solar-calibrated mixing length $\alpha_{MLT} = 2.0$. Both the Gray and Phoenix models of atmosphere prefer lower mixing length values while the Krishna Swamy model of atmosphere prefers higher mixing length values when fit to M92. The resulting double-peak feature is shown in Figure 11.

To determine which MC parameters are most important for determining the uncertainty in the age estimate for M92, the error budget for each parameter was calculated. For all the MC parameters in Table 1, along with distance modulus and reddening, we performed a maximum likelihood estimation using the weighted least square regression method, including the calculation of the covariance matrix. The estimate of the error contributed from each MC parameter is shown in Figure 13. Parameters that contribute less than 0.05% are
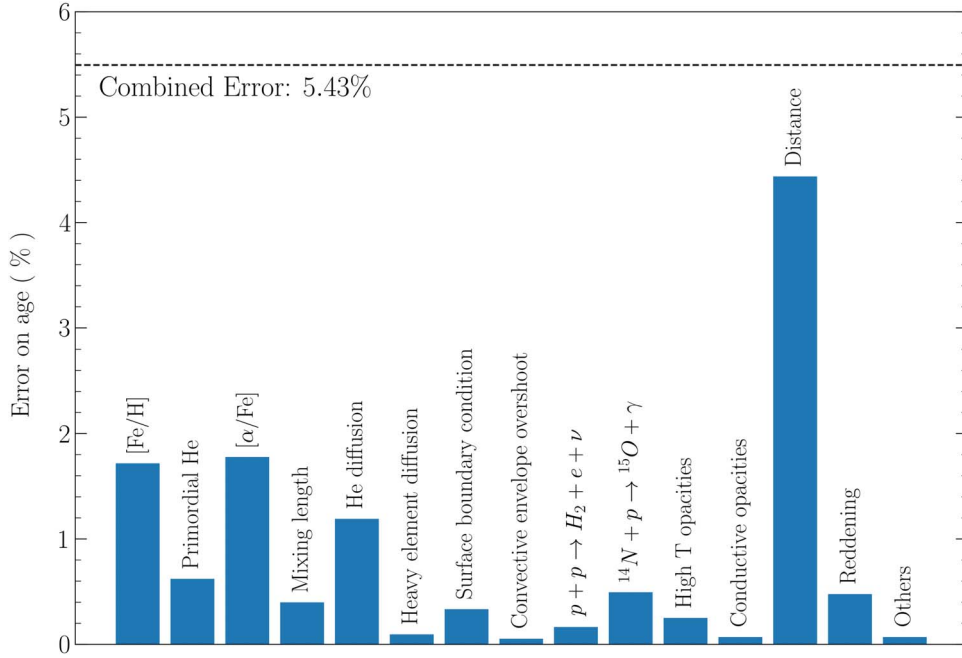
Figure 13. Contributions to the error of the age of M92 from each Monte Carlo parameter with distance modulus and reddening. The covariance and parameters that contribute less than 0.05% (i.e., less than 1% of the total error budget) are combined as "others". All the errors are converted to the percentage of the age of M92. The black dotted line represents the combined age error of 5.43%.
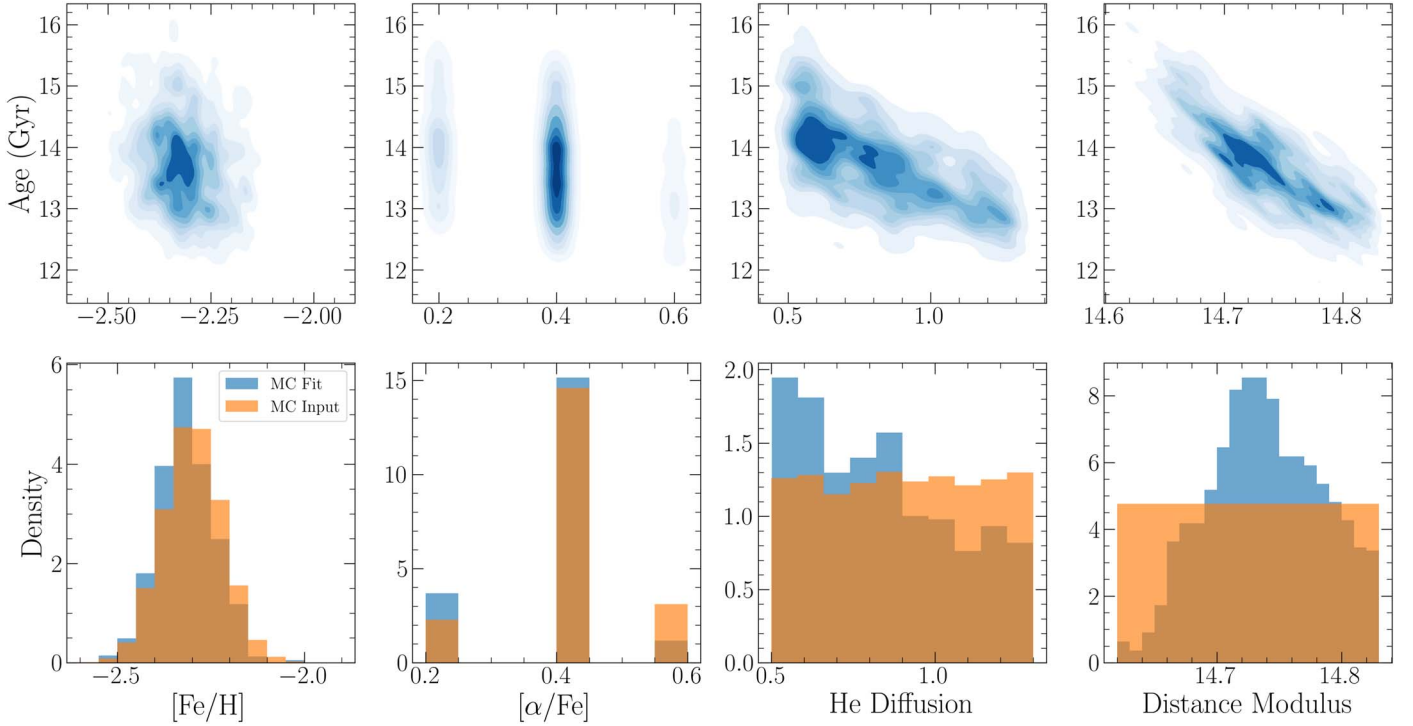

Figure 14. Distribution (bottom panels) of the four parameters with >1% (or ≳140 Myr) contribution to the age error from Figure 13 and their correlation with the measured age (top panels). Orange histograms represent the input distribution corresponding to Table 1 and blue histograms show the distribution of corresponding MC parameters from the 1100 best-fit isochrones.

combined as "others" and their contribution could be the result of their correlation with other parameters. The distance modulus is the dominant source of error.

Since the distance modulus parameter contributes most to the error and might dominate other parameters the value of the distance modulus and reddening was fixed, and the maximum likelihood estimation was repeated without those two

parameters. The result shows a similar contribution from each MC parameter that agree with Figure 13. The four MC parameters which contribute the most to the error budget were selected and their correlation with estimated age is shown in Figure 14. There is no significant correlation between [Fe/H] and age. This is because M92 has a relatively well-determined [Fe/H] value, and since it is very metal poor, the uncertainty in

the log-scaled [Fe/H] corresponds to a small change in the mass fraction of heavy elements (Z). There is a negative correlation between [α/Fe] and age, as best-fit isochrones prefer a lower α abundance which leads to a higher estimated age. The helium diffusion coefficient has an MC distribution that is weighted toward a somewhat smaller value than was found in Thoul et al. (1994) and displays an anticorrelation with age.

6. Conclusion

We determine the age of M92 using a statistical approach with Monte Carlo simulations which takes into account the uncertainties in the theoretical stellar evolution models and isochrones along with the observed uncertainties in the distance modulus, reddening, and composition of M92. We created 20,000 sets of Monte Carlo input parameters with 20 variables, which were used to generate 20,000 sets of theoretical isochrones over an abundance range of $-2.40 \leqslant$ [Fe/H] $\leqslant -2.20$ dex. We use DSEP to construct a set of isochrones from 8 Gyr to 16 Gyr with 0.2 Gyr increment for each set of input parameters. Each isochrone is calibrated using HIP 46120 and HIP 106924, two single, main-sequence stars with accurate colors and absolute magnitudes from HST ACS photometry and Gaia EDR3 parallaxes.

Each calibrated isochrone is used to generate an sCMD with 4,000,000 data points. Using the Voronoi Binning method, 800 bins are generated for each sCMD. HST ACS data for M92 is fit by each set of Voronoi bins with a shift in distance modulus ranging from 14.62 to 14.82 with an increment of 0.01, and reddening ranged from 0.0 to 0.05 with an increment of 0.01. A χ^2 goodness-of-fit parameter was calculated (see Equation (3)) and compared to the empirical χ^2 distribution generated using HST ACS data combined with an artificial star test.

We find that 1100 isochrones from the 20,000 sets of isochrones constructed were within 3σ of the mean of the empirical distribution. The age of M92 is determined by the mean age of the 1100 isochrones, weighted by the result from single star calibrations and χ^2 comparison. We find the age of M92 to be 13.80 ± 0.75 Gyr, an error of 5.4%. The dominant contributor to this uncertainty is the distance modulus, with the metallicity, α enhancement, and treatment of helium diffusion being the other sources of non-negligible error. The fact that the distance to M92, and not stellar physics, dominates the uncertainty points to the importance of precise and accurate distance measurements for further improvements in absolute age measurements. In future papers, we will present absolute age measurements for additional metal-poor GCs and their implications for our understanding of stellar physics and cosmology.

ORCID iDs

Jiaqi (Martin) Ying ⦿ https://orcid.org/0009-0006-5300-2976
Brian Chaboyer ⦿ https://orcid.org/0000-0003-3096-4161
Emily M. Boudreaux ⦿ https://orcid.org/0000-0002-2600-7513
Catherine Slaughter ⦿ https://orcid.org/0000-0002-5752-3780
Michael Boylan-Kolchin ⦿ https://orcid.org/0000-0002-9604-343X
Daniel Weisz ⦿ https://orcid.org/0000-0002-6442-6030

References

Acharya, B., Carlsson, B. D., Ekström, A., Forssén, C., & Platter, L. 2016, PhLB, 760, 584
Adelberger, E. G., García, A., Robertson, R. G. H., et al. 2011, RvMP, 83, 195
Anderson, J., Sarajedini, A., Bedin, L. R., et al. 2008, AJ, 135, 2055
Arnold, J. A., Romanowsky, A. J., Brodie, J. P., et al. 2011, ApJL, 736, L26
Aver, E., Olive, K. A., & Skillman, E. D. 2015, JCAP, 2015, 011
Baumgardt, H., & Vasiliev, E. 2021, MNRAS, 505, 5957
Bica, E., & Alloin, D. 1986, A&A, 162, 21
Brown, T. M., Tumlinson, J., Geha, M., et al. 2014, ApJ, 796, 91
Canuto, V. 1970, ApJ, 159, 641
Cappellari, M., & Copin, Y. 2003, MNRAS, 342, 345
Carretta, E., Bragaglia, A., Gratton, R., D'Orazi, V., & Lucatello, S. 2009, A&A, 508, 695
Carretta, E., Gratton, R. G., Clementini, G., & Pecci, F. F. 2000, ApJ, 533, 215
Cecco, A. D., Becucci, R., Bono, G., et al. 2010, PASP, 122, 991
Chaboyer, B. 1996, NuPhS, 51, 10
Chaboyer, B., & Kim, Y.-C. 1995, ApJ, 454, 767
Chaboyer, B., McArthur, B. E., O'Malley, E., et al. 2017, ApJ, 835, 152
Chakraborty, S., deBoer, R., Mukherjee, A., & Roy, S. 2015, PhRvC, 91, 045801
Claret, A. 2004, A&A, 424, 919
Cohen, J. G. 2011, ApJL, 740, L38
Collaboration, G., Brown, A. G. A., Vallenari, A., et al. 2021, A&A, 649, A1
deBoer, R. J., Görres, J., Smith, K., et al. 2014, PhRvC, 90, 035804
Demarque, P., Woo, J.-H., Kim, Y.-C., & Yi, S. K. 2004, ApJS, 155, 667
Dotter, A., Chaboyer, B., Jevremović, D., et al. 2008, ApJS, 178, 89
Ebrahimi, H., Sollima, A., Haghi, H., Baumgardt, H., & Hilker, M. 2020, MNRAS, 494, 4226
Eddington, A. S. 1926, The Internal Constitution of the Stars (Cambridge: Cambridge Univ. Press)
Ferguson, J. W., Alexander, D. R., Allard, F., et al. 2005, ApJ, 623, 585
Gaia Collaboration, Brown, A. G. A., Vallenari, A., et al. 2021, A&A, 649, A1
Haft, M., Raffelt, G., & Weiss, A. 1994, ApJ, 425, 222
Hauschildt, P. H., Allard, F., & Baron, E. 1999, ApJ, 512, 377
Hubbard, W. B., & Lampe, M. 1969, ApJS, 18, 297
Iglesias, C. A., & Rogers, F. J. 1996, ApJ, 464, 943
Irwin, A. W. 2012, FreeEOS: Equation of State for stellar interiors calculations, Astrophysics Source Code Library, ascl:1211.002
Joyce, M., & Chaboyer, B. 2018, ApJ, 856, 10
Kraft, R. P., & Ivans, I. I. 2003, PASP, 115, 143
Krishna Swamy, K. S. 1966, ApJ, 145, 174
Lin, M., Lucas, H. C., & Shmueli, G. 2013, Information Systems Research, 24, 906
Lindegren, L., Klioner, S. A., Hernández, J., et al. 2021a, A&A, 649, A2
Lindegren, L., Bastian, U., Biermann, M., et al. 2021b, A&A, 649, A4
Marcucci, L. E., Schiavilla, R., & Viviani, M. 2013, PhRvL, 110, 192503
Marín-Franch, A., Aparicio, A., Piotto, G., et al. 2009, ApJ, 694, 1498
Marta, M., Formicola, A., Bemmerer, D., et al. 2011, PhRvC, 83, 045804
Mészáros, S., Martell, S. L., Shetrone, M., et al. 2015, AJ, 149, 153
Milone, A. P., Piotto, G., Bedin, L. R., et al. 2012, A&A, 540, A16
Milone, A. P., Piotto, G., Renzini, A., et al. 2017, MNRAS, 464, 3636
Mowla, L., Iyer, K. G., Desprez, G., et al. 2022, ApJL, 937, L35
Mowlavi, N., Eggenberger, P., Meynet, G., et al. 2012, A&A, 541, A41
O'Malley, E. M., McWilliam, A., Chaboyer, B., & Thompson, I. 2017, ApJ, 838, 90

Paust, N. E. Q., Reid, I. N., Piotto, G., et al. 2010, AJ, 139, 476
Pietrinferni, A., Cassisi, S., Salaris, M., & Castelli, F. 2004, ApJ, 612, 168
Riess, A. G., Casertano, S., Yuan, W., et al. 2021, ApJL, 908, L6
Roederer, I. U., & Sneden, C. 2011, AJ, 142, 22
Salaris, M., & Weiss, A. 2002, A&A, 388, 492
Sarajedini, A., Bedin, L. R., Chaboyer, B., et al. 2007, AJ, 133, 1658
Taylor, M. B. 2005, in ASP Conf. Ser. 347, Astronomical Data Analysis Software and Systems XIV, ed. P. Shopbell, M. Britton, & R. Ebert (San Francisco, CA: ASP), 29

Thoul, A. A., Bahcall, J. N., & Loeb, A. 1994, ApJ, 421, 828
VandenBerg, D. A., Denissenkov, P. A., & Catelan, M. 2016, ApJ, 827, 2
VandenBerg, D. A., Richard, O., Michaud, G., & Richer, J. 2002, ApJ, 571, 487
Weisz, D. R., McQuinn, K. B. W., Savino, A., et al. 2023, arXiv:2301.04659
Xu, Y., Takahashi, K., Goriely, S., et al. 2013, NuPhA, 918, 61
Zinn, J. C. 2021, AJ, 161, 214